Long-Term dynamical Evolution of High Area-to-Mass Ratio Debris Released in GEO

Yehia A. Abdel-Aziz, A.M. Abdelaziz, and S. K. Tealib
Aton Space Technology, Masdar City, Abu Dhabi, UAE

Abstract

Studying the dynamics of high area-to-mass ratio objects in near-geostationary Earth Orbit (GEO) is crucial for understanding their nature, orbital evolution, and potential origins, which are essential for space situational awareness. This paper presents a numerical propagator developed to model the long-term behavior of space objects with a high area-to-mass ratio in GEO while accounting for relevant perturbations. The dynamical assessment utilized ephemeris data from the Vimpel catalog and compared it with the numerical propagator results. The study investigated the long-term dynamical behavior of space debris with varying high area-to-mass ratios, confirming that our numerical propagator's trajectory matched the Vimpel catalog data. However, some cases revealed differences in dynamical behavior between the numerical integrators and the ephemeris data. Overall, the results suggest that space debris with a high area-to-mass ratio in GEO can persist in space for several decades, maintaining a mean motion close to the original orbit while displaying significant eccentricity and semi-major axis variations.

Keywords: Long-term, solar radiation pressure, third-body perturbations.

1. Introduction

Many geostationary objects are likely the result of multiple explosions in spacecraft and upper stages, though the exact number remains unknown. Optical observations help identify numerous decimeter-sized objects within geostationary orbits. Recent optical observations have unveiled the intricate influence of solar radiation pressure on faint, uncatalogued objects, particularly those characterized by high area-to-mass ratios. This phenomenon notably alters the eccentricity and semi-major axis of geostationary Earth orbit (GEO) satellites, with minimal impact on the overall energy of their orbital paths. The discernible effects are most pronounced in objects exhibiting elevated area-to-mass ratios (Anselmo and Pardini, 2010). Eccentricity and inclination cause different amplitudes in the cumulative mean variations of the semi-major axis during eclipse seasons (Valk and Lemaitre, 2008). Früh and Schildknecht (2011) investigated the temporal variations in area-to-mass ratios and orbital parameters of objects observed optically over several years. Their study encompassed objects located at various sites, providing valuable insights into the dynamic evolution of these parameters. The outcomes unveiled a time-dependent variation in the scaling factor of the direct radiation pressure parameter. Intriguingly, the magnitude of the change in the area-to-mass ratio did not exhibit a correlation with the magnitude of its associated error, indicating a complex and nuanced relationship between these parameters. Rosengren and Scheeres (2013) studies on the dynamics of high area-to-mass ratio objects, conducted since their discovery in near-GEO orbits, have been crucial for understanding their nature, orbital evolution, and possible origins, which are essential for space situational awareness. Analyzing the orbital evolution of the mean eccentricity for the Two-Line Elements (TLE) set of the Molniya satellite constellation reveals that the lunisolar effect significantly affects the behavior of the longitude of the ascending node and the argument of pericenter (Alessi et al., 2021). In nominal mission scenarios, geostationary satellites perform end-of-life orbit maneuvers to reach suitable disposal orbits where they do not interfere with operational satellites (Proietti et al., 2021). Orbital prediction accuracy varies for optical observations due to the inaccuracy of the NORAD catalog information used; this discrepancy arises from the time difference between the observation and the epoch time of the TLE (Abdelaziz et al., 2022). Currently, there are 8 analysis centers within the International Laser Ranging Service (ILRS) responsible for releasing precise orbit products for the two LAGEOS satellites. However, there is a notable absence of research focused on analyzing the consistency of these orbits (Zhou et al., 2024). In orbit determination, when comparing Extended Kalman Filters (EKF) with Unscented Kalman Filters (UKF), the unscented semi-analytical Kalman filter provided more accurate orbital state estimates and required less time and fewer observations to converge (Tealib et al., 2023).

The primary objective of this paper is to explore viable model approximations capable of accurately 'reconstructing' the mean evolution of orbital eccentricity as derived from observational data. Our approach seeks to establish a synergistic relationship between observed dynamics and mathematical modeling. Specifically, we delve into the long-term evolution of spacecraft in Highly Elliptical Orbits (HEOs). In our analysis, we consider only natural perturbations affecting the spacecraft, including solar radiation pressure (SRP), anomalies in the Earth's gravitational field, and gravitational interactions induced by third bodies, namely the Sun and the Moon.

2. Exploring Dynamic Models for the Long-Term Evolution

This section presents a comprehensive explanation of the equations of motion within the geocentric coordinate system. Let $\mathbf{r}$ denote the position vector and $\ddot{\mathbf{r}}$ the velocity vector. We formulate the Hamiltonian function considering the gravitational attraction of the central body and the J_2 perturbation (Abdel-Aziz, 2013). This involves expressing the intricate relationship between the position, velocity, and the Hamiltonian function, shedding light on the impact of central-body gravitation and the J_2 perturbation on the orbital dynamics.

We can express the Hamiltonian function as follows: (Vallado, 2013).

$$F_0 = -\frac{\mu^2}{2L^2} - R(L, G, H, l, g, h) \tag{1}$$

The Delaunay variables of the Hamiltonian can be expressed as: (Abdel-Aziz, 2013)

$$L = \sqrt{\mu a}, \quad G = L\sqrt{1-e^2}, \quad H = G\cos i, \quad l = M, \quad g = \omega \quad h = \Omega. \tag{2}$$

L, a direct function of energy; H, representing the magnitude of angular momentum; and G, denoting the angular momentum projected onto the z-axis.

Here, $a, e, i, \Omega, \omega,$ and M represent the semi-major axis, eccentricity, orbit inclination, right ascension of ascending node, argument of perigee, and mean anomaly of the orbit, respectively.

The perturbing potential due to the second zonal harmonic arises from gravitational interactions and Earth's oblateness. This perturbation affects the system's dynamics by influencing orbital elements, thus impacting the spacecraft's long-term trajectory evolution. The expression for this potential can be described as follows (Tealib et al, 2020):

$$R = -\frac{\mu}{r} J_2 \left(\frac{\mathrm{R_e}}{r}\right)^2 \left(\frac{3}{2}\sin^2\phi - \frac{1}{2}\right) \tag{3}$$

where J$_2$ is the second zonal harmonic coefficient, and μ is the gravitational constant.

We can represent this function in terms of orbital elements using

$$\sin^2\phi = \frac{1}{2}\sin^2 i\left[1-\cos 2(g+f)\right] \tag{4}$$

Where *f* is a true anomaly.

The orbital dynamics equation is formulated by expressing it as a function that integrates different orbital elements. This equation provides into the interdependence of these elements and reveals the impact of external influences, such as the second zonal harmonic, on the spacecraft's trajectory over time. Explicitly expressing the orbital dynamics equation, we obtain: (Zhao et al., 2019)

$$\begin{cases} \dot{g}_0 = \dfrac{\partial F_0}{\partial G} = -\dfrac{3\mu^4 J_2}{2G^6 L^3}(G^2 - 5H^2) \\ \dot{h}_0 = \dfrac{\partial F_0}{\partial H} = -\dfrac{3\mu^4 J_2 H}{G^5 L^3} \\ \dot{l}_0 = \dfrac{\partial F_0}{\partial L} = n + \dfrac{3nJ_2}{2(1-e^2)^{3/2} a^2}(3\cos^2 i - 1) \\ \dfrac{\partial F_0}{\partial l} = \dfrac{\partial F_0}{\partial g} = \dfrac{\partial F_0}{\partial h} = 0 \end{cases}$$

(5)

where 'n' represents the mean motion.

3. Orbital Dynamics under Radiative Forces

The acceleration caused by solar radiation pressure is closely tied to a satellite's mass and surface area. It is crucial to consider both factors when studying the impact of solar radiation pressure on a satellite's orbit. The relationship between mass and surface area affects how the satellite reacts to radiation, determining its path and behavior over time in space.

$$F_{srp} = c_r p_r \frac{A}{m} a_s^2 r r_s \cos\phi_s \tag{6}$$

Here, C_r denotes the coefficient of reflection from the satellite's surface, $p_r = 4.56\times10^{-6} N/m^2$ the vector from the Earth to the Sun, and $\boldsymbol{r}_s$, the mean distance from the Earth to the Sun.

The osculating functions that define the immediate orbital parameters change when affected by Solar Radiation Pressure (SRP). These adjusted functions reflect how radiative forces, satellite properties, and changing orbital elements interact dynamically. Integrating SRP-induced changes improves the accuracy of depicting the satellite's path, considering the ongoing impact of solar radiation on orbital movements.

$$\begin{cases} \dot{l}_{srp} = \dfrac{\partial F_{srp}}{\partial L} = 2C_r P_r \dfrac{A}{m}\dfrac{L}{\mu}\left[u\left(\xi_1\overline{r}_{s,1} + \xi_2\overline{r}_{s,2} + \xi_3\overline{r}_{s,3}\right) + v\left(\eta_1\overline{r}_{s,1} + \eta_2\overline{r}_{s,2} + \eta_3\overline{r}_{s,3}\right)\right] \\ \dot{L}_{srp} = \dfrac{\partial F_{srp}}{\partial l} = -C_r P_r \dfrac{A}{m}\dfrac{a}{\left(1 - ecosE\right)} \\ \qquad \left[-\left(\xi_1\overline{r}_{s,1} + \xi_2\overline{r}_{s,2} + \xi_3\overline{r}_{s,3}\right)\sin E + \left(\eta_1\overline{r}_{s,1} + \eta_2\overline{r}_{s,2} + \eta_3\overline{r}_{s,3}\right)\sqrt{1-e^2}\cos E \right] \\ \dot{g}_{srp} = \dfrac{\partial F_{srp}}{\partial G} = C_r P_r \dfrac{A}{m}\dfrac{G}{e\mu}\left[\left(\xi_1\overline{r}_{s,1} + \xi_2\overline{r}_{s,2} + \xi_3\overline{r}_{s,3}\right) + \dfrac{e\sin E}{\sqrt{1-e^2}}\left(\eta_1\overline{r}_{s,1} + \eta_2\overline{r}_{s,2} + \eta_3\overline{r}_{s,3}\right)\right] \\ \dot{G}_{srp} = -\dfrac{\partial F_{srp}}{\partial g} = -C_r P_r \dfrac{A}{m} a\left[-\dfrac{\partial \xi}{\partial \omega} u\,\mathrm{s} + \dfrac{\partial \eta}{\partial \omega} v \right] \\ \dot{h}_{srp} = \dfrac{\partial F_{srp}}{\partial H} = -\dfrac{C_r P_r A a(\dfrac{\partial \xi}{\partial i} u + \dfrac{\partial \eta}{\partial i} v)}{mG\sin i} \\ \dot{H}_{srp} = -\dfrac{\partial F_{srp}}{\partial h} = C_r P_r \dfrac{A}{m} a(\dfrac{\partial \xi}{\partial \Omega} u + \dfrac{\partial \eta}{\partial \Omega} v) \end{cases} \tag{7}$$

Equ. (7) describes the osculating functions in the presence of Solar Radiation Pressure (SRP). These equations provide the partial derivatives of the disturbing function F_{srp} for various orbital elements.

Where:

$C_r$is the radiation pressure coefficient.

$P_r$is the solar radiation pressure at 1 AU.

A/m is the area-to-mass ratio of the satellite.

μ is the standard gravitational parameter.

a, e, E are the semi-major axis, eccentricity, and eccentric anomaly.

ζ_r, η_r are components related to the satellite's orientation and solar radiation impact.

l, L, g, G, h, H are the osculating elements related to the satellite's orbit.

u,v are variables representing additional terms related to the forces acting on the satellite.

4. The Gravitational Effects of the Moon and Sun on Orbital Dynamics

The intricate influences of third-body perturbations are frequently elucidated through potential expansion in series, emphasizing the correlation between orbital dimensions and the distance from the third body. This approach is used to study the acceleration of smart dust particles under the gravitational influence of the Sun, especially when considering the subtle effects of Luni-solar perturbations. (Abdelaziz et.al 2021). Understanding how orbital characteristics interact with third-body perturbations helps us grasp the intricate paths celestial objects follow in these gravitational environments.

$$F_{ls}=\frac{\mu_{ls}\left(\mathbf{r}_{ls}-\mathbf{r}\right)}{\left\|\mathbf{r}_{ls}-\mathbf{r}\right\|^{3}}-\frac{\mu_{ls}\left(\mathbf{r}_{ls}\right)}{\left\|\mathbf{r}_{ls}\right\|^{3}} \tag{8}$$

where μ_{ls} is the gravitational coefficient of the third body, $\mathbf{r}\ and\ \ \mathbf{r}_{ls}$ the position vectors of the satellite, and the third body for the central planet, respectively. The osculating functions under the effect of the third body can be written as

$$\begin{aligned}
\dot{l}_{ls} &= \frac{\partial F_{ls}}{\partial L}=\frac{\mu_{ls}}{r_{ls}^{3}}\left[\frac{6L^{3}}{\mu^{2}}\left(u\left(\xi_1\overline{r}_{s,1}+\xi_2\overline{r}_{s,2}+\xi_3\overline{r}_{s,3}\right)+\nu\left(\eta_1\overline{r}_{s,1}+\eta_2\overline{r}_{s,2}+\eta_3\overline{r}_{s,3}\right)\right)^{2}-\frac{2L^{3}}{\mu^{2}}(1-e\cos E)^{2}\right]\\
\dot{L}_{ls} &= \frac{\partial F_{ls}}{\partial l}=\frac{\mu_{ls}}{r_{ls}^{3}}\frac{a}{\left(1-ecosE\right)}\\
&\left[\begin{array}{l}\left(u\left(\xi_1\overline{r}_{s,1}+\xi_2\overline{r}_{s,2}+\xi_3\overline{r}_{s,3}\right)+\nu\left(\eta_1\overline{r}_{s,1}+\eta_2\overline{r}_{s,2}+\eta_3\overline{r}_{s,3}\right)\right)\\ \left(-\left(\xi_1\overline{r}_{s,1}+\xi_2\overline{r}_{s,2}+\xi_3\overline{r}_{s,3}\right)\sin E+\left(\eta_1\overline{r}_{s,1}+\eta_2\overline{r}_{s,2}+\eta_3\overline{r}_{s,3}\right)\sqrt{1-e^{2}}\cos E\right)-re\sin E\end{array}\right]\\
\dot{g}_{ls} &= \frac{\partial F_{ls}}{\partial G}=\frac{\mu_{ls}}{r_{ls}^{3}}\frac{G}{\mu e}\left[-\frac{3a\left(u\left(\xi_1\overline{r}_{s,1}+\xi_2\overline{r}_{s,2}+\xi_3\overline{r}_{s,3}\right)+\nu\left(\eta_1\overline{r}_{s,1}+\eta_2\overline{r}_{s,2}+\eta_3\overline{r}_{s,3}\right)\right)}{\sqrt{1-e^{2}}}+r\cos E\right]\\
\dot{G}_{ls} &= \frac{\partial F_{ls}}{\partial l}=\frac{3\mu_{ls}}{r_{ls}^{3}}a^{2}\left[\left(u\left(\xi_1\overline{r}_{s,1}+\xi_2\overline{r}_{s,2}+\xi_3\overline{r}_{s,3}\right)+\nu\left(\eta_1\overline{r}_{s,1}+\eta_2\overline{r}_{s,2}+\eta_3\overline{r}_{s,3}\right)\right)\left(-\frac{\partial\xi}{\partial\omega}u+\frac{\partial\eta}{\partial\omega}\nu\right)\right]\\
\dot{h}_{ls} &= \frac{\partial F_{ls}}{\partial H}=-\frac{3\mu_{ls}a^{2}}{r_{ls}^{3}}\left(u\left(\xi_1\overline{r}_{s,1}+\xi_2\overline{r}_{s,2}+\xi_3\overline{r}_{s,3}\right)+\nu\left(\eta_1\overline{r}_{s,1}+\eta_2\overline{r}_{s,2}+\eta_3\overline{r}_{s,3}\right)\right)(\frac{\partial\xi}{\partial i}u+\frac{\partial\eta}{\partial i}\nu)\\
\dot{H}_{ls} &= -\frac{\partial F_{ls}}{\partial h}=\frac{9\mu_{ls}a^{2}}{r_{ls}^{3}}(\frac{\partial\xi}{\partial\Omega}u+\frac{\partial\eta}{\partial\Omega}\nu)\left(u\left(\xi_1\overline{r}_{s,1}+\xi_2\overline{r}_{s,2}+\xi_3\overline{r}_{s,3}\right)+\nu\left(\eta_1\overline{r}_{s,1}+\eta_2\overline{r}_{s,2}+\eta_3\overline{r}_{s,3}\right)\right)
\end{aligned} \tag{9}$$

where

η,ξ: Coefficients related to the third body's gravitational influence.

$\overline{r}_{s,1}$: Components of the perturbing force due to the third body in the xxx-direction.

The equations provided represent the effects of a third body's gravitational influence on a spacecraft's orbital elements. These equations are derived from the perturbation theory, specifically focusing on how the third body's gravity alters the spacecraft's orbit. Each term corresponds to a specific change in the orbital elements, accounting for the complex interactions between the spacecraft, the central body (Earth), and the third body (e.g., the Moon or the Sun).

The osculating functions change due to the gravity of a third body, representing dynamic variables that summarize the changing orbital parameters. This change is described through a series expansion, showing the complex link between orbit features and the effects caused by the third body. The resulting equations offer a detailed understanding of how celestial objects' trajectories and orbital elements evolve as they move through the gravitational fields of main bodies and their perturbations.

5. Result and discussion

In this section, we conducted numerical simulations and compared them with observational data to gain valuable insights into the dynamics of space objects in Highly Elliptical Orbits (HEOs). The analysis primarily examined the impact of different perturbations, such as J_2 effects, solar radiation pressure, and the gravitational forces from the Moon and the Sun.

5.1 The Relationship between Area-to-Mass Ratio and Orbital Dynamics.

This section examines the semi-major axis distribution and its correlation with area-to-mass ratio and inclination over two days. The analysis is centered on data from the GEO region sourced from the Russian catalog at the JSC Vimpel site (http://spacedata.vimpel.ru). Fig. 1 shows two scatter plots comparing the Semi-Major Axis Distribution with Area-to-Mass Ratio and Inclination for data sourced from the GEO region, as per the Russian catalog at the JSC Vimpel site.

We partitioned the figure into two segments, with the first part depicting data from June 14, 2016, labeled as Part A. Approximately 600 objects were utilized in this analysis. The semi-major axis spans a range of 36,000 to 50,000 km. notably, the density of objects is higher within the area-to-mass ratio (AMR) range of 0.06 to 10 $m^2\ kg^{-1}$, coupled with inclinations up to 15 degrees. In the region where the area-to-mass ratio (AMR) values range from 10 to 20 $m^2\ kg^{-1}$, the distribution is comparatively sparse, coinciding with an increase in inclination angles up to 35 degrees. Objects exhibiting an area-to-mass ratio from 20 to 40 $m^2\ kg^{-1}$ extend their distribution up to a radius of 49,000 km, with inclination angles surpassing 40 degrees. This observation suggests a distinctive arrangement of objects with AMR values and inclination angles, highlighting the nuanced dynamics within this specific orbital parameter space. In the subsequent period, Part B on June 24, 2021, witnessed a substantial increase in the number of space objects, totaling nearly 1,600 from 2008 until June 2021. A comparative analysis of the data collected in 2016 (Part A) and 2021 (Part B) reveals a notable shift. The majority of objects in 2021 are concentrated within an area-to-mass ratio ranging from 10 to 40 $m^2\ kg^{-1}$, with a semi-major axis span of 36,000 to 48,000 km. additionally, the inclination remains within 40 degrees, with an eccentricity of 0.7. This comparison underscores the evolving distribution of space objects over time, highlighting key changes in orbital parameters and population density. Now, we utilize the initial conditions and orbital elements for actual Highly Elliptical Orbits (HEO) as presented in Table 1. The first column enumerates the Space Objects (SO), which remains constant for a specific object across a series of publications. The subsequent columns detail the date of the first measurement for each object (day, month, year), followed by the semi-major axis of the orbit (a) km, eccentricity (e), orbit inclination (i) degree, and the area-to-mass ratio (m^2/kg). It's essential to note that the orbital parameters provided are osculating Keplerian elements and the coordinate system is referenced to the epoch J2000.

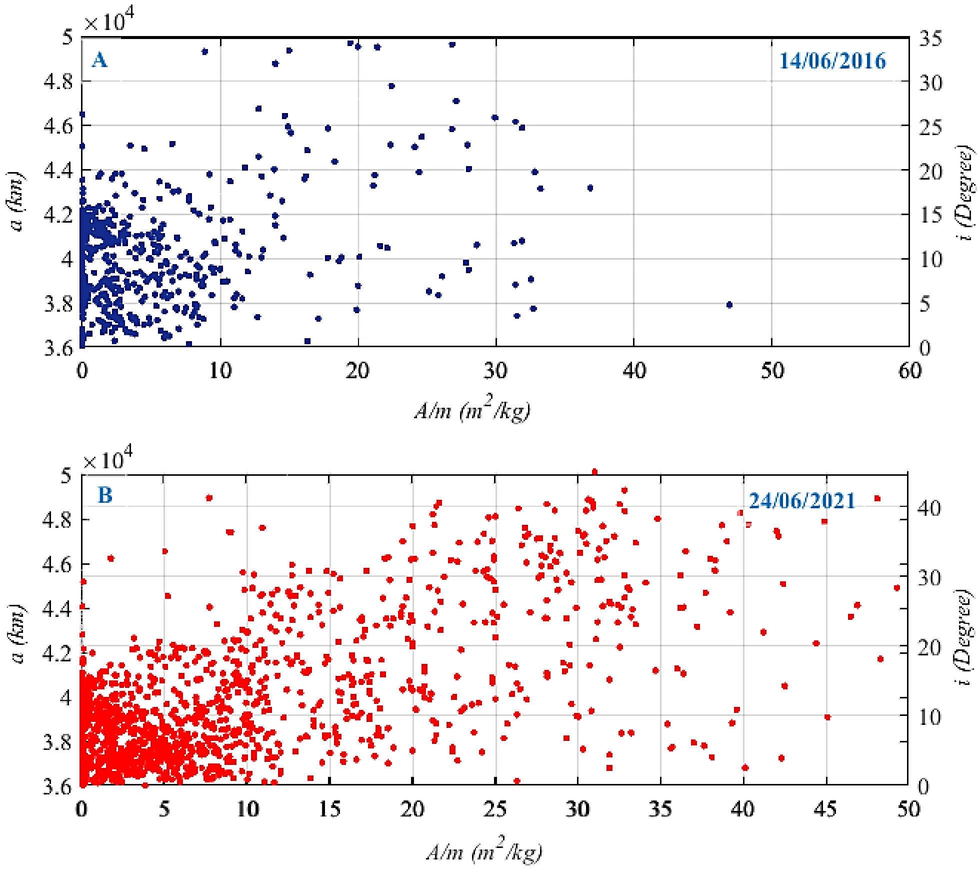

Fig. 1 Semi-Major Axis Distribution with Area-to-Mass Ratio and Inclination.

Table 1. Initial conditions for simulations

No. SO	date of the first measurement	Semi-major axis (a) km	Eccentricity	Inclination (*i*) degree	area-to-mass ratio (A/m) m2/kg
138900	09/03/2013	41236	0.2541	1.343	5.2
97200		32514.5	0.158382	9.973	13
143108	10/03/2011	42070.5	0.090292	8.635	20
138800	8062008	40612.8	0.730831	31.907	38
139501	1032011	41335.5	0.241764	11.91	11
140006	10042015	41086.1	0.570524	17.402	40
142107	22092015	41832.7	0.2	2.14	8.7
143312	31102012	42217.3	0.141887	21.476	19.4
97100	2112015	42352.2	0.231424	9.715	12

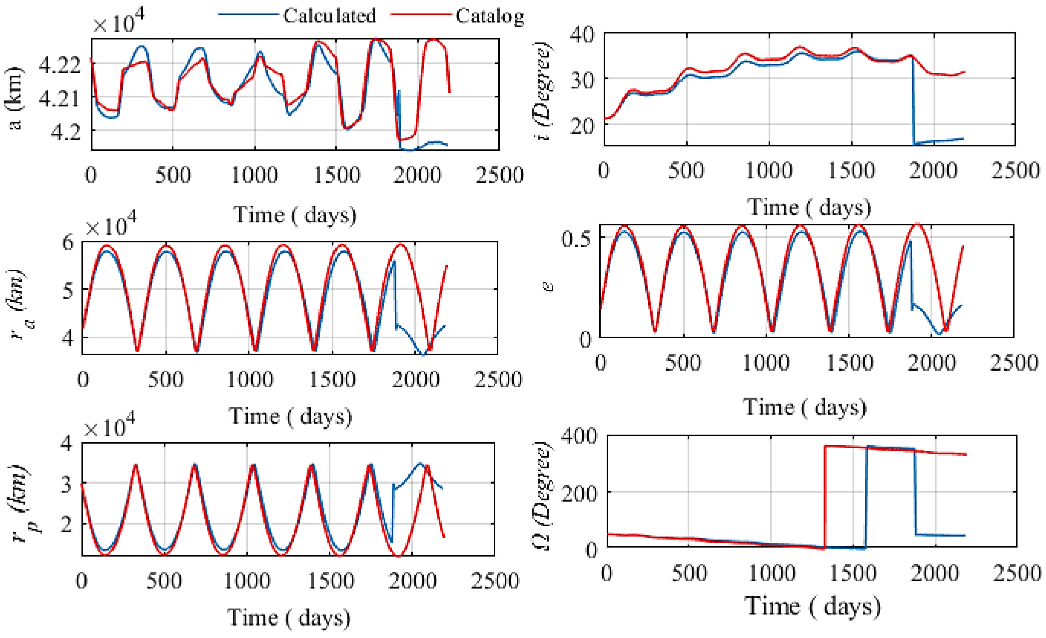

Fig. 2 Comparative Analysis of Numerical Propagation and Catalog for Orbital Elements

Fig. 2 shows the numerical Propagation of SO 143312 Object (Table 1) from 2016 to 2021, considering various influences such as J_2, solar radiation pressure, and third-body attractions from the Moon and the Sun. The graphs compare calculated data (blue curve) with catalog data (red curve) and illustrate the variations in different orbital parameters over time. The plot illustrates variations in the semi-major axis (a), apogee, perigee, inclination, eccentricity, and right ascending node. The initial inclination of 21.4 degrees undergoes significant changes, reaching a maximum of 35.14 degrees after 5 years of integration. This leads to significant annual fluctuations in the semi-major axis, initially ranging from a minimum of 42,050 km to a maximum of 42,250 km. Over time, the semi-major axis undergoes additional variations, oscillating between 42,280 km and 41,950 km.

5.2 Investigating the Evolutionary Trajectory of Space Objects in Highly Elliptical Orbits.

In this section, the long-term orbit evolution of GEO satellites is investigated using the equations of motion introduced in Section 3. The perturbations included in the physical model are central-body gravitation and J_2 perturbation, the third-body pull of the Moon and Sun, and the solar radiation pressure. Fig. 3 provides a comprehensive overview of the average behavior orbital parameters over a 6-year simulation period, considering varying area-to-mass ratios (Am = 5, 13, 20, 38 m^2/kg). Each curve, depicted in blue, green, red, and purple, corresponds to a distinct aspect ratio. The eccentricity, inclination, apogee, perigee, and semi-major axis collectively contribute to understanding the orbital dynamics. Notably, the figure unveils an intriguing relationship between the area-to-mass ratio and the inclination of the orbit. As the area-to-mass ratio increases, the inclination exhibits a discernible pattern. For instance, at an Am of 5 m^2/kg, the inclination decreases from 2 to 0.3 before gradually rising to 10 degrees. In contrast, at an Am of 38 m^2/kg, the inclination first decreases from 32 to 3, then undergoes a gradual increase to 33, followed by a reduction to 2 degrees. This intricate behavior in inclination emphasizes the sensitivity of the orbital dynamics to variations in the area-to-mass ratio. The observed trends contribute valuable insights into the complex interplay between these parameters and their cumulative impact on the long-term evolution of the orbital track.

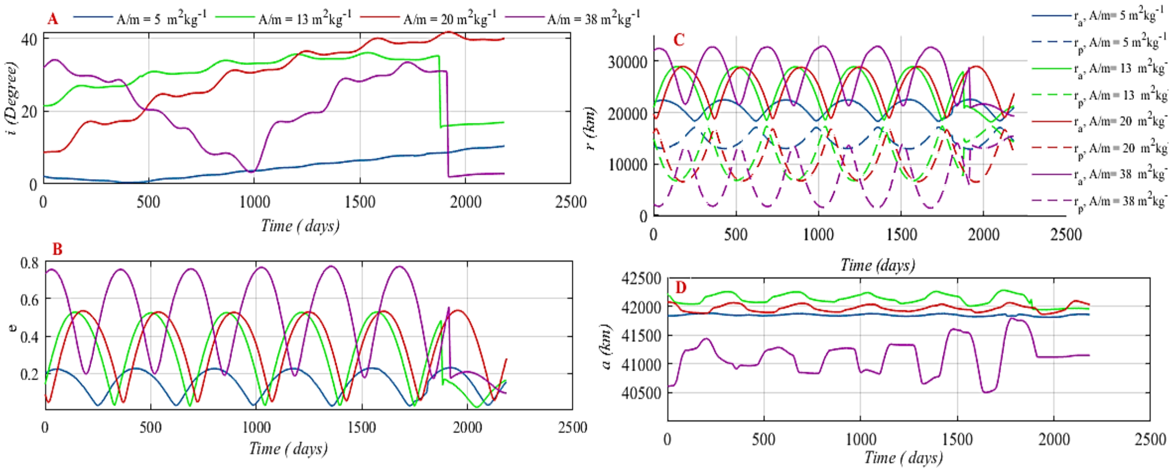

Fig. 3: Long-Term Evolution of Orbital Elements over a 6-year simulation period

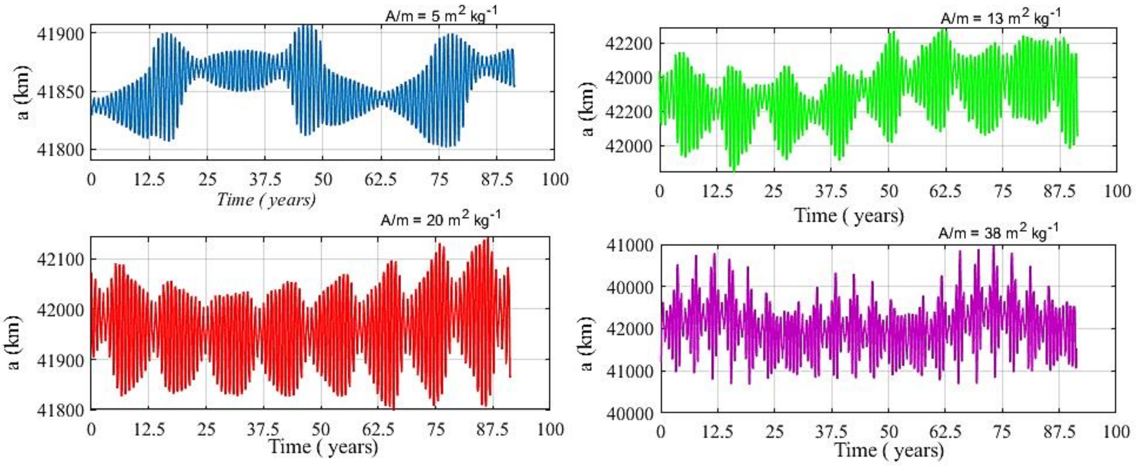

Fig. 4. Long-Period Evolution of the Semi-Major Axis

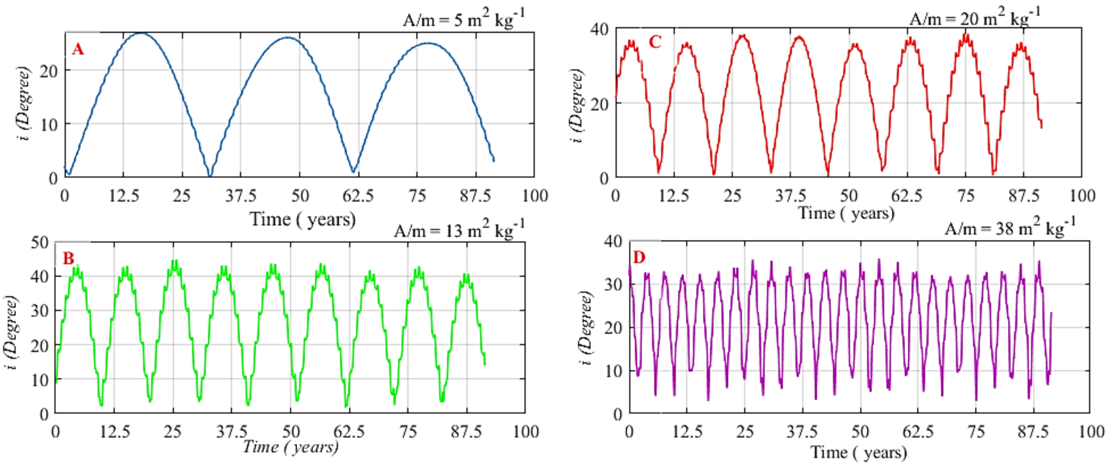

Fig. 5. Long-Period Evolution of Inclination

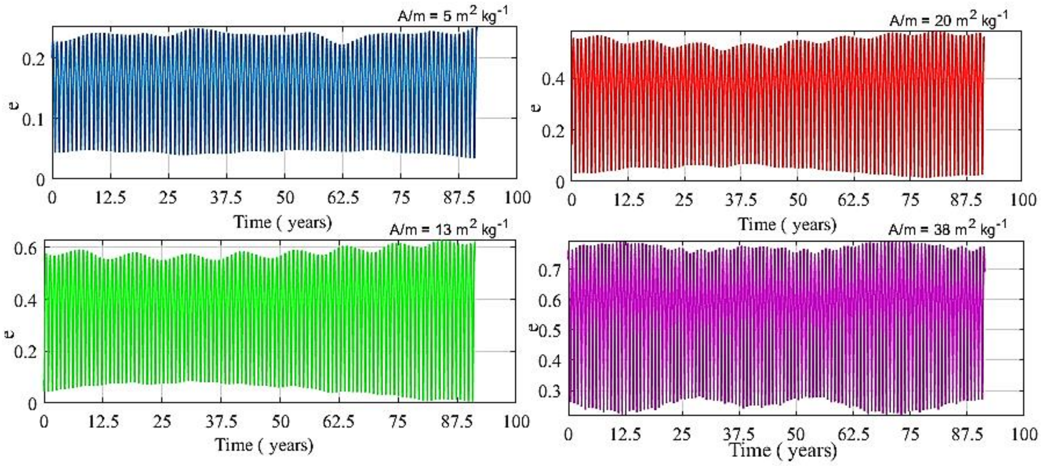

Fig. 6. Long-Period Evolution of Eccentricity

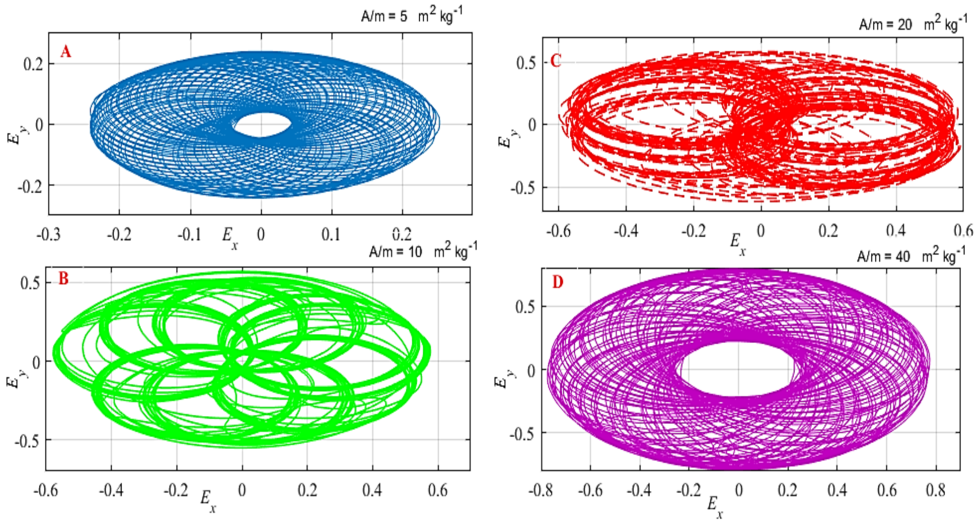

Fig.7. Evolution of Eccentricity for Different Area-to-Mass Ratios Over 100 Years

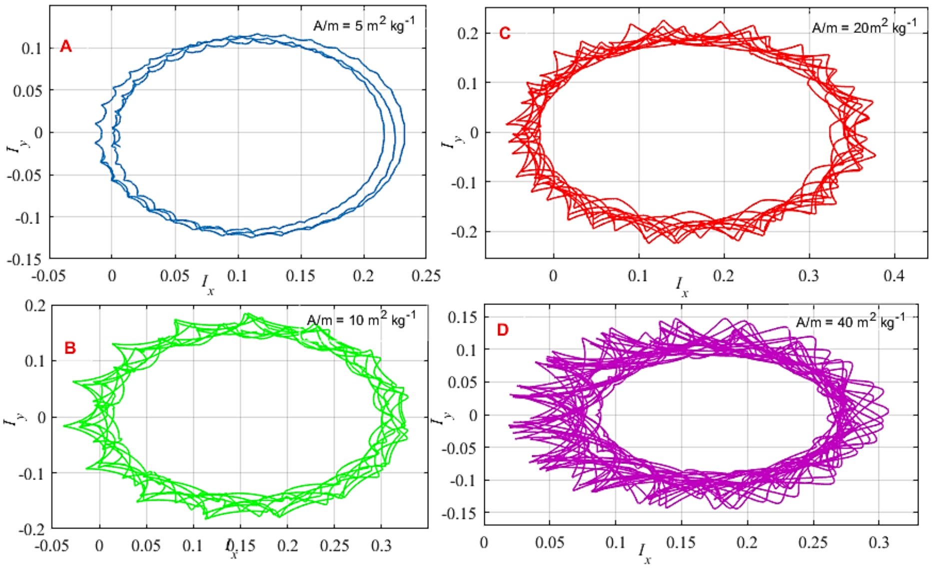

Fig.8 Evolution of inclination for Different Area-to-Mass ratios over 100 Years

The range of eccentricity curves exhibits a gradual increase across different area-to-mass ratios. Specifically, at 5 m²/kg, the amplitude spans from 0.003 to 0.2, extending to 0.02 to 0.5 at 13 m²/kg, 0.05 to 0.53 at 20 m²/kg, and 0.1 to 0.75 at 38 m²/kg, ultimately evolving from 0.17 to 0.5. Over an extended period of 100 years, as depicted in Figs. 4, 5, and 6, the amplitude values for eccentricity undergo notable changes: 0.03 to 0.25 at 5 m²/kg, 0.008 to 0.6 at 13 m²/kg, 0.02 to 0.57 at 20 m²/kg, and 0.2 to 0.78 at 38 m²/kg. Simultaneously, the average inclination values experience a significant transformation throughout the extended timeframe. Initially ranging from 24 to 25 degrees at 5 m²/kg, the average inclination shifts to 30 to 39 degrees at 13 m²/kg, 35 to 37 degrees at 20 m²/kg, and 22 to 31 degrees at 38 m²/kg. These variations contribute to the accelerated changes in the semi-major axis, indicating the dynamic nature of the orbital evolution over an extended period. These figures demonstrate the significant impact of the area-to-mass ratio on the long-term stability and behavior of orbital elements. In general, an increase in the area-to-mass ratio leads to greater and more chaotic changes over time across all orbital elements (semi-major axis, inclination, and eccentricity). Conversely, lower area-to-mass ratios correspond to more stable orbital elements with smaller variations.

Fig.7. presents the long-term evolution of orbital eccentricity for various area-to-mass ratios (A/m) over 100 years. Each subplot (A, B, C, D) corresponds to a specific area-to-mass ratio, demonstrating the evolution of eccentricity components E_y relative to E_x. In the first case (subplot A, Blue) at A/m = 5 (m² kg⁻¹), the evolution of eccentricity is represented by a compact and consistent pattern centered on the origin. This indicates that for a low area-to-mass ratio, the orbit experiences minimal perturbations, leading to relatively stable eccentricity over the observed period. In the second case (Subplot B, Green) at A/m = 10 (m² kg⁻¹), the trajectory becomes more dispersed, displaying significant oscillations compared to subplot A, due to the increased A/m ratio leading to greater sensitivity to perturbations and noticeable changes in orbital eccentricity. In the third case (Subplot C, Red) at A/m = 20 (m² kg⁻¹), the pattern becomes more complex and expansive, indicating substantial variations in eccentricity due to the higher A/m ratio significantly amplifying perturbative effects and resulting in pronounced fluctuations in eccentricity. Finally, in Subplot D (Purple) at A/m = 40 (m² kg⁻¹), the trajectory is the most spread out and intricate among the four subplots, demonstrating very large variations in eccentricity. This high A/m ratio makes the orbit highly susceptible to perturbations, leading to dramatic changes in eccentricity over time. Fig.8. illustrates the long-term evolution of orbital inclination for different area-to-mass ratios (A/m) over 100 years. In subplot A (Blue) at A/m = 5 (m² kg⁻¹), the inclination evolution follows a tight, nearly elliptical pattern, indicating minimal perturbations and relatively stable inclination over time due to the low area-to-mass ratio. In subplot B (Green) at A/m = 10 (m² kg⁻¹), the trajectory shows more pronounced oscillations compared to subplot A, signaling greater sensitivity to perturbations caused by the increased area-to-mass ratio. Subplot C (Red) at A/m = 20 (m² kg⁻¹) exhibits a wider and more complex pattern, suggesting significant variations in inclination due to the higher area-to-mass ratio amplifying perturbative effects. Finally, in Subplot D (Purple) at A/m = 40 (m² kg⁻¹), the trajectory displays the most spread out and intricate pattern among the four subplots, demonstrating significant fluctuations in inclination. The high area-to-

mass ratio makes the orbit highly susceptible to perturbations, resulting in dramatic changes in inclination over time. This analysis effectively demonstrates the impact of varying area-to-mass ratios on the long-term stability of a spacecraft's orbital inclination. Understanding these dynamics is crucial for the design and management of space missions, especially those involving small satellites.

6. **Conclusion**

This study delves into the long-term evolutions of space objects in geostationary orbits, considering the influential factors of J_2 term, Solar Radiation Pressure (SRP), and three-body gravitational interactions. The investigation employs actual space objects with diverse Area-to-Mass ratios, utilizing data from the Russian catalog obtained from the JSC Vimpel site. The initial exploration focuses on the distribution of the semi-major axis as a function of area-to-mass ratio and inclination. The findings reveal a crowded range of semi-major axis from 36,000 to 42,000 km, particularly for objects with area-to-mass ratios less than 10 $m^2\ kg^{-1}$. The study proceeds to assess the accuracy of numerical propagation under perturbation forces by comparing the results with data from the catalog over 6 years. Subsequently, the feasibility of solving the averaged problem exactly in closed form is demonstrated for a cannonball model, predicting significant variations in eccentricity and inclination over short periods. Further analysis explores the amplitudes and periods of secular perturbations in both short and long-term propagations, highlighting their dependency on the magnitude of the Area-to-Mass ratio (A/m) values and initial orbital conditions. The observed variations in eccentricity, inclination, and semi-major axis underscore the complex and dynamic nature of the orbital evolution influenced by perturbation forces. Comparisons with the Vimpel catalog validate the general behavior of the numerical results, affirming the significance of solar radiation pressure as a primary factor influencing the dynamic behaviors of these objects. While some differences exist, the overall consistency with the catalog findings reinforces the understanding that solar radiation pressure plays a crucial role in shaping the long-term evolution of space objects in geostationary orbits. Finally, an increase in the area-to-mass ratio is associated with a more chaotic and expansive evolution of eccentricity, leading to greater orbital perturbations. Orbits with higher area-to-mass ratios are more sensitive to external forces, resulting in larger fluctuations in eccentricity. The varying area-to-mass ratios significantly impact the long-term stability of a spacecraft's orbit. Understanding these dynamics is crucial for designing and managing space missions, especially those involving small satellites or space debris with high area-to-mass ratios.

References

Abdelaziz, A. M., Tealib, S. K., & Molotov, I. 2021. Analytical study of Egyptian TIBA-1 satellite orbit from Optical Satellite Tracking Station (OSTS), NRIAG-Egypt. Astrophysics and Space Science, 366(8). https://doi.org/10.1007/s10509-021-03987-7

Abdelaziz, A. M., Ibrahim, M., Liang, Z., Dong, X., & Tealib, S. K. 2022. Orbit Predictions for Space Object Tracked by Ground-Based Optical and SLR Stations. Remote Sensing, 14(18), 4493. https://doi.org/10.3390/rs14184493

Abdel-Aziz YA. An analytical theory for avoidance collision between space debris and operating satellites in LEO. Applied Mathematical Modelling [Internet]. 2013 Oct; 37(18–19):8283–91. Available from: http://dx.doi.org/10.1016/j.apm.2013.03.045

Alessi EM, Buzzoni A, Daquin J, Carbognani A, Tommei G. Dynamical properties of the Molniya satellite constellation: Long-term evolution of orbital eccentricity. Acta Astronautica [Internet]. 2021 Feb;179:659–69. Available from: http://dx.doi.org/10.1016/j.actaastro.2020.11.047

Anselmo L, Pardini C. Long-term dynamical evolution of high area-to-mass ratio debris released into high earth orbits. Acta Astronautica [Internet]. 2010 Jul;67(1–2):204–16. Available from: http://dx.doi.org/10.1016/j.actaastro.2009.10.017

Früh C, Schildknecht T. Variation of the area-to-mass ratio of high area-to-mass ratio space debris objects. Monthly Notices of the Royal Astronomical Society [Internet]. 2011 Nov 29;419(4):3521–8. Available from: http://dx.doi.org/10.1111/j.1365-2966.2011.19990.x

Proietti S, Flores R, Fantino E, Pontani M. Long-term orbit dynamics of decommissioned geostationary satellites. Acta Astronautica [Internet]. 2021 May;182:559–73. Available from: http://dx.doi.org/10.1016/j.actaastro.2020.12.017

Rosengren AJ, Scheeres DJ. Long-term dynamics of high area-to-mass ratio objects in high-Earth orbit. Advances in Space Research [Internet]. 2013 Oct;52(8):1545–60. Available from: http://dx.doi.org/10.1016/j.asr.2013.07.033

Tealib SK, Abdel-Aziz YA, Awad MES, Khalil I, Radwan M. Satellite formation flying control using an innovative technique subject to electromagnetic acceleration. International Journal of Space Science and Engineering [Internet]. 2020;6(2):147. Available from: http://dx.doi.org/10.1504/ijspacese.2020.110360

Tealib SK. Accurate High-Altitude Orbit Determination Method using Electro-Optical Sensors. International Journal of Mathematics and Physics [Internet]. 2023 Dec;14(2). Available from: http://dx.doi.org/10.26577/ijmph.2023.v14.i2.08

Valk S, Lemaître A. Semi-analytical investigations of high area-to-mass ratio geosynchronous space debris including Earth’s shadowing effects. Advances in Space Research [Internet]. 2008 Oct;42(8):1429–43. Available from: http://dx.doi.org/10.1016/j.asr.2008.02.010

Vallado, D.A.: Fundamentals of Astrodynamics and Applications. McGraw-Hill, New York .2013. ISBN: 1881883183, 9781881883180

Zhao, Y., Feng, D., Sun, S., & Zhao, Y. 2019. Research on High Area-to-Mass Ratio Satellite Dynamics. Proceedings of 2019 Chinese Intelligent Systems Conference, 718–726. https://doi.org/10.1007/978-981-32-9698-5_78

Zhou, C., Wang, J., Zhong, S., Peng, B., Zhang, J., Han, J., & Guo, Z. 2024. Validation of long arc orbit determination method based on orbital residuals analysis and determination of coordinates of Chinese SLR stations using the LAGEOS satellites. Advances in Space Research, 73(8), 4226–4240. https://doi.org/10.1016/j.asr.2024.01.012

http://spacedata.vimpel.ru